Argon-Milling-Induced Decoherence Mechanisms in Superconducting Quantum Circuits

J. Van Damme[1,2,*] Ts. Ivanov,[1] P. Favia,[1] T. Conard,[1] J. Verjauw,[1,3] R. Acharya,[1,2]
D. Perez Lozano,[1] B. Raes,[4] J. Van de Vondel,[4] A.M. Vadiraj,[1] M. Mongillo,[1] D. Wan,[1]
J. De Boeck,[1,2] A. Potočnik,[1,†] and K. De Greve[1,2]

[1]*Imec, Kapeldreef 75, Leuven, B-3001, Belgium*

[2]*Department of Electrical Engineering (ESAT), KU Leuven, Leuven, B-3000, Belgium*

[3]*Department of Materials Engineering (MTM), KU Leuven, Leuven, B-3000, Belgium*

[4]*Department of Physics and Astronomy, KU Leuven, Leuven, B-3000, Belgium*

The fabrication of superconducting circuits requires multiple deposition, etching, and cleaning steps, each possibly introducing material property changes and microscopic defects. In this work, we specifically investigate the process of argon milling, a potentially coherence-limiting step, using niobium and aluminum superconducting resonators as a proxy for the surface-limited behavior of qubits. We find that niobium microwave resonators exhibit an order of magnitude decrease in quality factors after surface argon milling, while aluminum resonators are resilient to the same process. Extensive analysis of the niobium surface shows no change in the suboxide composition due to argon milling, while two-tone spectroscopy measurements reveal an increase in two-level system electrical dipole moments, indicating a structurally altered niobium oxide. However, a short dry etch can fully recover the argon-milling-induced losses on niobium, offering a potential route towards state-of-the-art overlap Josephson junction qubits with niobium circuitry.

I. INTRODUCTION

Superconducting quantum circuits show great promise for the realization of quantum information processors. The technology offers design flexibility with a variety of structures like capacitors, inductors, resonators, and Josephson junctions (JJs) that can be combined into complex systems. However, there are still multiple hurdles ahead on the road towards further upscaling and useful applications, with material imperfections being one of the principal challenges to address [1,2]. Superconducting quantum devices suffer from undesired relaxation and decoherence through interactions with two-level systems (TLSs) formed by defects residing in amorphous materials, oxides, and interfaces surrounding the superconductors [3,4]. Limited qubit coherence impacts gate fidelities and requires more extensive error-correction schemes. Additionally, these same TLSs are responsible for random temporal fluctuations in qubit parameters, requiring active feedback and tuning [5–7]. In large superconducting quantum processors, such frequent recalibrations of the system will lead to

an enormous overhead. It is therefore paramount to better understand the origins of TLS defects and develop appropriate fabrication processes with suitable materials to minimize them.

Decades of experimental research into the elusive TLS defects has revealed their predominant location to be at the outer surfaces and interfaces of the devices [8–11]. Advances in substrate cleaning prior to metal deposition have successfully reduced losses at the substrate-metal interface [12–14], while surface oxide removal experiments [15,16] have demonstrated the importance of substrate-air and metal-air interfaces. Another important consideration is the impact of fabrication processes on the creation of defects in different materials. Ion milling is a fabrication process of interest, often used to improve Ohmic contacts between two metal layers, or during the fabrication of a JJ with an overlap process [17–19] to remove the native aluminum oxide (caused by the vacuum break between bottom- and top-electrode patterning) prior to controlled barrier formation. Previous works have shown that substrate cleaning with ion milling prior to metal deposition degrades the metal-substrate interface [12,14,20,21]. Global surface ion milling in high vacuum or NH_3-passivated environments [22] can increase resonator losses and reduce qubit lifetimes, indicating that the

*jacques.vandamme@imec.be

†anton.potocnik@imec.be

metal-air and/or substrate-air interfaces can be negatively altered by ion milling. However, the underlying nature of the milling-induced losses is not entirely clear. Additionally, the effect of an oxidized ion-milled superconductor, which is unavoidable for the fabrication of overlap JJs [17–19], has not been adequately studied.

All state-of-the-art qubits are currently fabricated with $Al/AlO_x/Al$ JJs [23,24]. However, other circuitry like capacitor pads, feedlines, and resonators are often fabricated from other superconducting materials in favor of higher superconducting critical temperatures T_c (like Nb [14]), or low-loss, self-limiting native oxide properties (like TiN [25] or Ta [23]). In this work, we characterize argon-milling-induced substrate-air and metal-air interface losses on two of the most frequently used superconducting materials: niobium and aluminum. Since superconducting qubits and resonators share the same surface loss mechanism, resonators are often used as a "short-loop" proxy to study surface and interface losses in qubits [20, 26]. We fabricate superconducting resonators and subject them to different argon-milling conditions. We characterize and compare their microwave loss mechanisms and analyze corresponding material changes with scanning transmission electron microscopy (STEM), energy dispersive x-ray analysis (EDS), electron energy-loss spectroscopy (EELS), atomic force microscopy (AFM), x-ray photoelectron spectroscopy (XPS), and temperature dependencies. We find that aluminum devices are not affected significantly by the argon-milling conditions, while niobium devices exhibit an order of magnitude increase in microwave loss. We provide evidence for the creation of TLSs with increased dipole moments inside the argon-damaged niobium oxide.

II. EXPERIMENT DESCRIPTION

In this study we conduct material loss investigation using planar, lumped-element resonators (LERs) inside a three-dimensional superconducting cavity. In contrast to more widely used coplanar waveguide (CPW) resonators [27,28], LERs provide the possibility to characterize individual chips that undergo multiple iterations of surface treatments, since no adhesion or wire bonding is required [15]. Each chip holds six LERs with different designs (labeled as Res 1–6, and 3.9–5.5 GHz) placed in an aluminum cavity (TE_{101} mode at 8 GHz) with adjustable input/output (I/O) ports for tuning the cavity-LER coupling. More information on the device designs can be found in Appendix B and in Ref. [15]. The resonance frequencies and quality factors of LERs are extracted by fitting a generalized Lorentzian model to the transmission scattering parameters S_{21} measured at 10 mK with a vector network analyzer (VNA). All reported fitting results are acquired with the PYTHON LMFIT package [29]. The experimental setup and the fitting model used for the
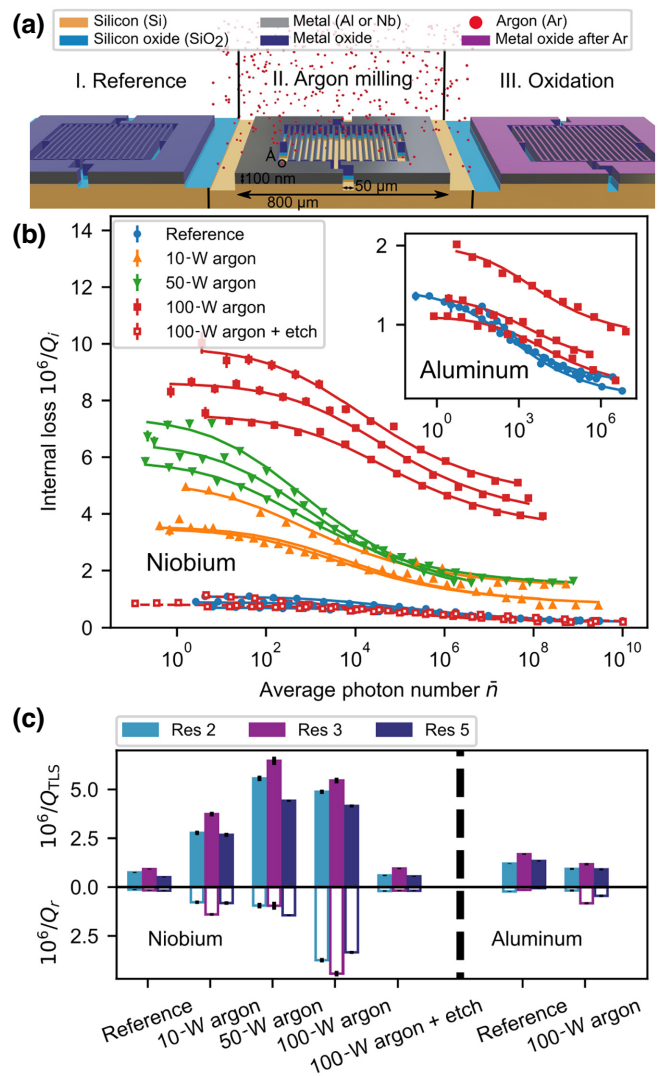

FIG. 1. (a) Schematic visualization of a cross section of a resonator undergoing surface argon-milling treatment followed by plasma oxidation. (b) Microwave power dependence of the internal losses $1/Q_i$ is compared between different samples that receive varying powers of argon milling before oxidation. The same three devices (Res 2, Res 3, and Res 5) of each sample are shown. Error bars correspond to one standard deviation uncertainty extracted from the resonator line shape fitting. Continuous lines are fits with Eq. (1). The main figure contains the niobium device data, the inset shows aluminum device data. (c) Two-level system loss ($1/Q_{TLS}$) and residual loss ($1/Q_r$) extracted from the power sweeps with error bars of one standard deviation in fitting parameter uncertainty.

cavity-coupled resonators are described in Appendices A and B, respectively.

The LER devices used in this study are fabricated on 300-mm wafers in the foundry-standard cleanroom at Imec [15]. High-resistivity (>3 kΩ cm) silicon substrates are cleaned with hydrofluoric (HF) acid prior to sputtering of 100-nm superconducting metal (either Nb or Al).

The devices are patterned with optical lithography using a SiO_2 hard mask and a chlorine based dry etch. After resist and hard mask removal, the wafers are coated with protective resist and diced (stripped with acetone afterwards). A 2-min oxygen ashing step is used to remove organic residues and to saturate oxide growth on all outer surfaces. This is the reference point for the argon-milling study (reference sample). Additional samples are further exposed to a chip-wide physical sputtering by argon plasma, generated using an rf field with a gas flow of 20 cm^3/min and a pressure of 4.6 mTorr (using a Pfeiffer Spider 630 tool). These samples are argon milled for 15 min with a split of plasma rf powers: 10, 50, or 100 W [Fig. 1(a)]. Here, the 100-W power setting is strong enough to fully consume the surface oxides of both aluminum and niobium and it corresponds to the overlap JJ fabrication condition described in Ref. [17]. The differently milled samples are, at the end, intentionally reoxidized with the same 2-min oxygen-ashing recipe, ensuring similar thickness surface oxides for the comparison of the argon-milling-introduced losses with those of the reference. The consumption of niobium or aluminum due to the argon milling is limited to 20 nm and the step into the silicon increases from approximately 50 to 100 nm. In addition, the niobium sample that is exposed to the 100-W argon treatment is, after characterization, further dry etched for 10 s with $SiCl_4$ to remove the argon-milled top layer, followed by 2 min of oxygen ashing. All differently treated LER samples and additional processing details are summarized in Table I.

The microwave losses of reference LER devices are limited by the surface interfaces, as illustrated by our previous work where removal of the surface oxides with HF reduced losses by almost an order of magnitude [15].

Therefore, any effect of the argon-milling treatments on the substrate-air and metal-air interfaces translate into observable changes in microwave loss. All differently treated LER samples shown in Table I are compared in terms of their microwave loss using single- and two-tone [30–32] microwave power saturation experiments at 10 mK inside a dilution refrigerator, as discussed in the following section. Certain samples are then selected for further surface analysis (indicated in Table I) based on their microwave losses.

III. RESULTS

A. Single-tone loss saturation spectroscopy

Superconducting resonators measured at millikelvin temperatures exhibit a microwave power-dependent loss due to their interaction with a bath of TLS defects [33]. All tunneling TLS defects couple to phonon modes, while the critical defects also have electrical dipole moments and therefore couple to the electrical fields of the resonators or qubits in their proximity [4,34,35]. TLSs form a loss channel that broadens the resonator linewidth, which is reflected in a reduced quality factor ($Q = f_r/\kappa$, with κ the full-width-at-half-maximum linewidth and f_r the resonator frequency). At elevated photon occupation in the resonator, TLSs with transition energies close to the LER's resonance are driven into saturation, a situation of equal population of ground and excited state, prohibiting them from absorbing more energy from the resonator. For a uniform energy distribution of TLSs, the quality factor dependence on photon number is described by Eq. (1), derived for noninteracting TLSs and uniform electrical

TABLE I. Overview of measured samples. From left to right: sample name, the substrate/metal stack, the processing performed on the device after fabrication, and the different types of characterizations performed on these samples. Single-tone (ST) saturation experiment, two-tone (TT) saturation experiment, STEM, XPS, AFM, and temperature dependence of resistance (on transport bridge device that received the same processing) and resonance frequency (see Appendix C).

| Name | Sub./met. | Processing | Performed characterization | | | | | |
			ST	TT	STEM	XPS	AFM	Temp.
Nb reference	Si/Nb	O_2 plasma (2 min)	x	x	x	x	x	x
Nb 10-W argon	Si/Nb	10-W argon milling (15 min) + O_2 plasma (2 min)	x	x		x		
Nb 50-W argon	Si/Nb	50-W argon milling (15 min) + O_2 plasma (2 min)	x	x		x		
Nb 100-W argon	Si/Nb	100-W argon milling (15 min) + O_2 plasma (2 min)	x	x	x	x	x	x
Nb 100-W argon + etch	Si/Nb	100-W argon milling (15 min) + O_2 plasma (2 min) + $SiCl_4$ etch (10 sec) + O_2 plasma (2 min)	x					
Al reference	Si/Al	O_2 plasma (2 min)	x	x				
Al 100-W argon	Si/Al	100-W argon milling (15 min) + O_2 plasma (2 min)	x	x				

fields ($\phi = 1$) [33],

$$\frac{1}{Q_i} = \frac{1}{Q_{\text{TLS}}} \frac{\tanh(hf_r/2k_BT)}{\sqrt{1 + (\bar{n}/n_c)^\phi}} + \frac{1}{Q_r}. \quad (1)$$

The contribution of the TLS to the total loss is captured by the parameter $1/Q_{\text{TLS}}$, $\bar{n}$ is the average photon number inside the resonator, n_c is the critical photon number governing the onset of TLS saturation, T is the temperature (10 mK), h is Planck's constant, k_B is the Boltzmann constant, and all residual (non-TLS) losses are represented in the parameter $1/Q_r$. Experimentally, one often finds a slower power dependence ($\phi < 1$) that is attributed to an interacting TLS model [36], or geometry-dependent electrical fields [37,38]. The inverse quality factors are measured as a function of microwave power on all samples in Table I. Results of three selected resonators (Res 2, Res 3, and Res 5) of each chip are shown in Fig. 1(b). The solid lines are fits with the TLS saturation model of Eq. (1) and the extracted loss parameters $1/Q_{\text{TLS}}$ and $1/Q_r$ are compared in Fig. 1(c) between samples. Our data fits well with a $\phi = 0.44 \pm 0.08$.

A striking difference is observed between the effect of argon milling on niobium and on aluminum resonators. The niobium resonators show an order of magnitude increase in loss between the reference sample and the 100-W argon sample, while aluminum shows resilience to the same process. Both TLS losses ($1/Q_{\text{TLS}}$) and microwave power-independent residual losses ($1/Q_r$) increase on niobium samples and scale with the milling power, illustrated in Figs. 1(b) and 1(c). Since both aluminum and niobium resonators are patterned on nominally identical high-resistivity silicon substrates, argon-milling-induced damage at the substrate-air interface can be ruled out as the dominant cause of increased microwave loss. Argon-milling-introduced losses must therefore originate from the niobium surface. This is further corroborated by a complete recovery of Q factors on niobium resonators where, after milling and oxidation, the top surface is removed with a 10-s dry etch [Nb 100-W argon + etch sample in Figs. 1(b) and 1(c)].

The niobium surface differs from the aluminum one in the complexity of the mixture of suboxides it can grow [39,40]. Aluminum has only the Al_2O_3 phase available at low energies, while native niobium surface oxide is usually a stack of NbO, NbO_2, and Nb_2O_5, which show superconductor ($T_c \cong 1.3$ K), semiconductor (gap of approximately 0.1 eV), and dielectric properties, respectively [16,39,41]. The different niobium oxides can cause microwave losses through a variety of mechanisms, for example, proximity effects of a surface metallic layer (e.g., NbO) [42] or an increase of quasiparticles due to magnetic impurities (e.g., paramagnetic interstitial oxygen and oxygen vacancies in Nb_2O_5) [43–46]. Additionally, the TLS defects hosted by the different suboxides could be drastically different. TLSs

in metallic glasses (like amorphous NbO) are expected to have orders of magnitude lower relaxation and coherence times due to additional scattering with electrons and would be more challenging to saturate [4]. Therefore, redistribution of the suboxides, structural reconfiguration of the suboxides, and incorporation of impurities are likely causing the observed argon-milling-induced losses. To investigate loss sources further, we next perform surface analysis with XPS and STEM on both the Nb reference sample and the Nb 100-W argon sample.

B. Niobium surface characterization

High-angle annular dark field (HAADF) STEM images of the cross section at the niobium-air interface show that the oxide layers before and after argon milling are of comparable thickness (about 4–5 nm) [Figs. 2(a) and 2(b)], indicating that the extra observed losses are intrinsic to the oxide layer and not skewed by potentially unequal amounts of lossy oxide. A striking difference is found in the appearance of layers showing different brightness in the argon-milled niobium oxide [Fig. 2(b)], indicative of a change in oxide density. The atomic concentrations extracted with EDS reveal a slight Si content (5.2 at. % in the oxide layer) in the argon-milled sample, which is likely sputtered onto the metal surface from the nearby exposed substrate area during the milling.

To further understand the difference between samples at the niobium-air interface, we perform EELS analysis on a cross section of the oxide layer, from which we extract the concentration ratio O:Nb [16,47], visualized by the color maps in Figs. 2(c) and 2(d). Both samples show NbO suboxide (ratio O:Nb ≤ 1) at the Nb interface and an increase in oxygen content when moving towards the surface, consistent with literature reports [15,16]. The argon-milled sample clearly exhibits a majority of Nb_2O_5 (O:Nb > 2) at the surface, while the reference sample EELS map displays a lower ratio O:Nb < 2, even at the top surface. However, surface sensitive XPS measurements [15,48] indicate a majority of Nb_2O_5 in all niobium samples, regardless of the argon-milling conditions [Fig. 2(f)]. The other suboxides (which are buried underneath the Nb_2O_5 top layer) show lower concentrations in XPS, and no clear correlation with the argon-milling power can be extracted. The inconsistency with the O:Nb < 2 EELS map on the reference sample is likely due to the higher surface roughness of the reference sample. Roughness along the focused ion beam (FIB) specimen thickness (around 40 nm) would intermix the detected signal of the thin oxide layer with the underlying niobium and the carbon on top, resulting in a reduced O:Nb ratio. This surface roughness would also explain the broadened concentration transitions at the interfaces seen in the EDS curves compared with the sharper transitions of the argon-milled sample with a smoother surface [Figs. 2(a) and 2(b)].
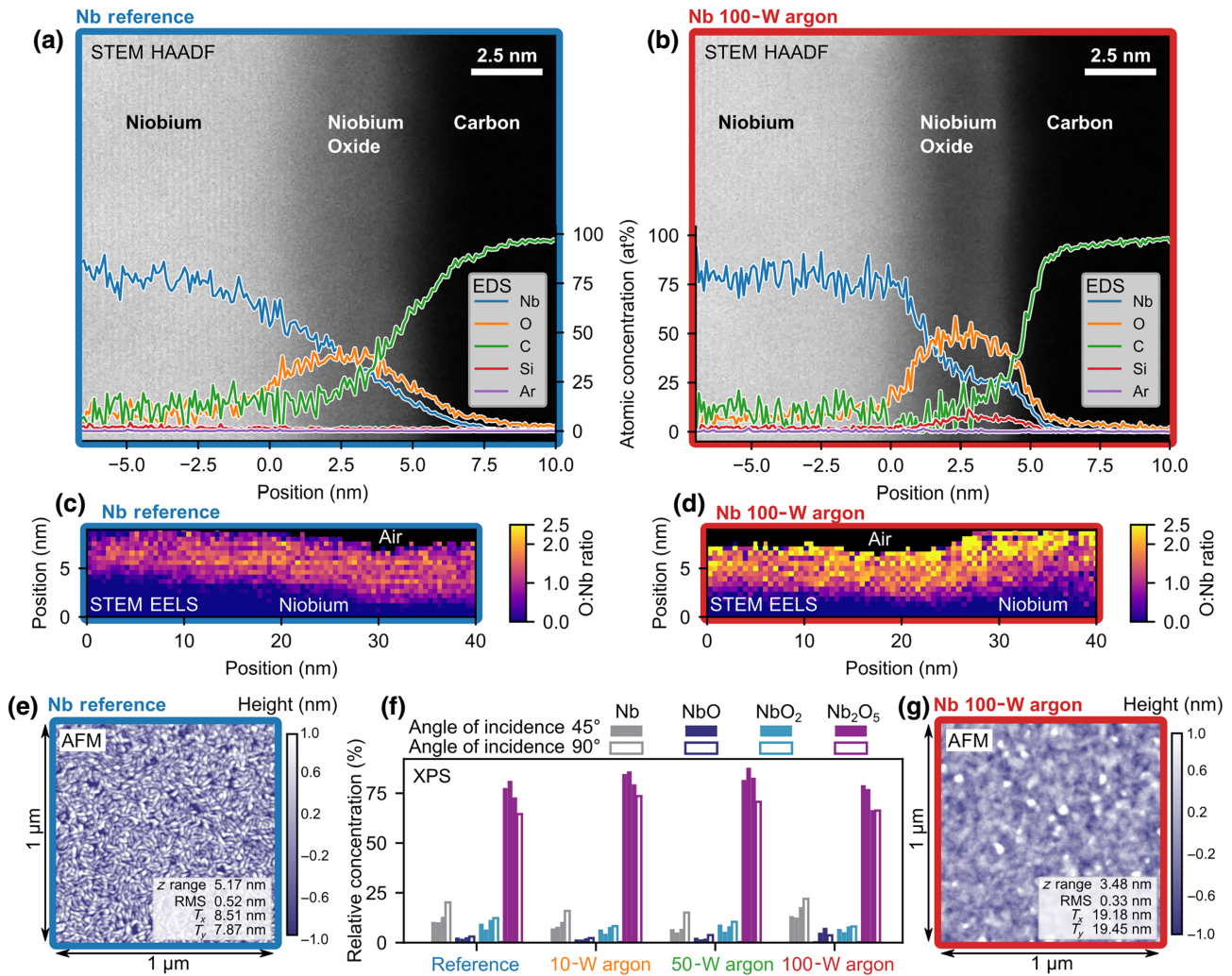
FIG. 2.   Niobium-air interface analysis of a reference sample (a),(c),(e),(f) and a sample that received the 100-W argon-milling treatment (b),(d),(f),(g). HAADF STEM images (a),(b) are shown together with atomic concentrations of various elements as a function of the cross-section depth (solid lines), extracted with EDS (20-nm-long region along Nb surface). EELS maps (c),(d) of the niobium-air interface cross section visualize the oxygen-to-niobium ratio throughout the oxide layer. The change in niobium surface topography due to the milling is visualized with the AFM images (e),(g), which show the maximal height difference (z range), roughness root-mean-square (RMS), horizontal, and vertical correlation lengths (T_x and T_y, respectively). Niobium suboxide concentrations for the four different argon-milling conditions are extracted by fitting to the Nb_{3d} XPS spectra (f), example shown in Appendix D. The corresponding measurement uncertainty is illustrated with multiple replicas of identically prepared samples (both resonator chips and blanket niobium chips).

AFM characterization of the reference and argon-milled surface topography corroborates this explanation. The argon milling smoothens the niobium surface, while simultaneously increasing valley and peak areas by a factor of 5.6, approximated from the change in horizontal and vertical surface height correlation lengths [Figs. 2(e) and 2(g)]. Surface roughness has been linked to increased loss due to enhanced participation ratio of the electric fields at the surface [49]. However, in our results, this effect is overshadowed by other loss contributions, as most losses are observed in the smoothest argon-milled sample.

Therefore, argon milling effectively smooths the niobium surface, and has little effect on the oxide layer's chemical composition apart from a slight increase in silicon content. The notable change in appearance revealed by the AFM and STEM images does indicate a change in roughness and density of the amorphous oxide layer as a consequence of niobium surface damage suffered during the milling. We revisit these findings and their possible implications in the discussion section. Additional information and details on the performed surface analysis methods can be found in Appendix D.

C. Two-tone spectroscopy

The surface characterization results incentivize further analysis techniques sensitive to microscopic defects created by the argon milling. More insight into the TLS contribution to the losses can be gained from two-tone saturation experiments [30–32], where one signal probes the resonator line shape, while another signal (pump) is used to saturate the TLS at the frequency of the pump tone. The latter can be detuned from the resonance frequency (f_r), analogous to spectral hole burning [50]. Each TLS coupled to the resonator causes a complex-valued frequency shift dependent on the TLS population, which can be calculated by means of adiabatic elimination [30,31],

$$\delta f_r = \sum_{j \in \{\text{TLS}\}} \frac{\Omega_{0,j}^2}{4} \frac{\langle \hat{\sigma}_z^{(j)} \rangle}{f_j - f_r + i\Gamma_2^{(j)}}, \qquad (2)$$

where hf_j, $\Gamma_2^{(j)}$, and $\Omega_{0,j}$ are the energy, decoherence rate, and coupling rate of the jth TLS coupled to the resonator. The imaginary part of the complex frequency shift corresponds to added losses and the real part is a change in resonance frequency. According to Eq. (2) saturated TLSs ($\langle \hat{\sigma}_z \rangle = 0$) do not add losses or frequency shifts to the resonator. The schematic in Fig. 3(a) illustrates how a resonance shift can be induced with a detuned pump tone. Assuming the standard tunneling model with a uniform energy distribution of TLSs [4], a weak probe, and strong pump signal, the resonator frequency shift becomes a function of pump frequency and power as described by Eq. (3) [30–32],

$$\delta f_r = \frac{3\sqrt{2}}{8} \frac{f_r \tanh(hf_r/k_B T)}{Q_{\text{TLS}}} \frac{\Delta}{\Omega_0 \sqrt{\bar{n}}} \frac{\sqrt{1 + (\Omega_0^2 \bar{n}/2\Delta^2)} - 1}{\sqrt{1 + (\Omega_0^2 \bar{n}/2\Delta^2)} + 1}, \qquad (3)$$

with experimentally tunable parameters $\Delta = f_{\text{pump}} - f_r$ the frequency detuning of the pump with the resonator, and $\bar{n}$ the average photon number inside the resonator due to the pump drive (photon number estimation is discussed in Appendix B). The resonator frequency shift depends on both the TLS loss ($1/Q_{\text{TLS}}$) and the average TLS single-photon Rabi frequency (Ω_0). The extrema of Eq. (3) are positioned at $\Delta = \mp\Omega_0 \sqrt{\bar{n}}/\sqrt{6}$, dependent on the coupling between resonator and the TLS.

The resonance shift δf_r as a function of pump detuning Δ is illustrated in Fig. 3(b). At every pump frequency, the line shape is probed with the VNA and the resonance frequency is determined. The average photon number $\bar{n}$ inside the resonator due to the pump at detuning Δ is estimated with Eq. (B5). The data is then fitted with Eq. (3), from which the fitting parameters $1/Q_{\text{TLS}}$ and Ω_0 are extracted.

All niobium devices show an additional frequency blue shift in Fig. 3(b) at small pump detuning, not captured by the model of Eq. (3). At large photon numbers (when driving close to resonance), the resonator sample locally heats up to temperatures $k_B T > hf_r$, thermally saturating the bath of TLSs. Equation (4) [33] explains the observed upwards frequency shift as a function of temperature (Ψ represents the digamma function). This temperature dependence is illustrated in Appendix C where the resonance frequency is plotted as a function of temperature for the niobium reference, and 100-W argon-milled samples. We add a term accounting for heating to Eq. (3) (post-fitting) to visualize it in the solid lines of Fig. 3(b),

$$\delta f_r(T) = \frac{f_r}{\pi Q_{\text{TLS}}} \text{Re}\left[\Psi\left(\frac{1}{2} - \frac{hf}{j\,2\pi k_B T} \right) - \ln\left(\frac{hf}{2\pi k_B T} \right) \right]. \qquad (4)$$

The extracted TLS loss component $1/Q_{\text{TLS}}$ measured for Res 2 on each sample is compared with up to three different experiments, labeled as single-tone, two-tone, and temperature [Fig. 3(c)]. The values compare reasonably well, and the observed variations are attributed to a variety of factors. In the two-tone experiment, a residual TLS saturation is caused by a finite probe power ($\bar{n} \approx 10^2$). Another cause for variation is a difference in sensitivity of resonance frequency and quality factor to the TLS bath. This comes from the different dependence of the real and imaginary parts of Eq. (2) on the TLS detuning ($f_j - f_r$). In the presence of a few dominant TLSs, or a nonuniform TLS energy distribution [51,52], this could result in a different $1/Q_{\text{TLS}}$ extracted from resonance frequency shifts δf_r compared to quality-factor data.

The average TLS single-photon Rabi frequency Ω_0 is plotted as a function of argon-milling power in Fig. 3(d). The model of Eq. (3) is sensitive to the product $\Omega_0 \sqrt{\bar{n}}$, with $\bar{n}$ estimated up to an uncertain proportionality factor (see Appendix B) translating into uncertainty of the absolute values of Ω_0. This does not change the qualitative result, nor any quantitative ratio comparisons between devices. The single-photon Rabi frequency is proportional to the electrical dipole moment $\left(h\Omega_0 \sqrt{\bar{n}} = \mathbf{E}_{\text{pump}} \cdot \mathbf{d} \right)$. Despite the estimated photon number uncertainty, we extract coupling rates of 20 kHz ($d/e \in [0.08; 8]$ nm as estimated in Appendix E, with e the elementary charge) for our reference samples, which are comparable to literature reports [30–32,53,55]. On the niobium devices, we observe an increase in dipole moments as a function of argon-milling power. In fact, the increase in dipole moments (up to a factor of 15 between the Nb reference and Nb 100-W argon-milled sample) exceeds the amount necessary to account for the observed loss $1/Q_{\text{TLS}} \propto d^2 N_0$, which is proportional to both the TLS density (N_0), and the dipole moment (d) squared [30]. Considering both Ω_0 and $1/Q_{\text{TLS}}$ in Figs. 3(c) and 3(d), we estimate a decrease in density of TLSs with respect to the reference sample $N_0/N_0^{\text{ref}} =$
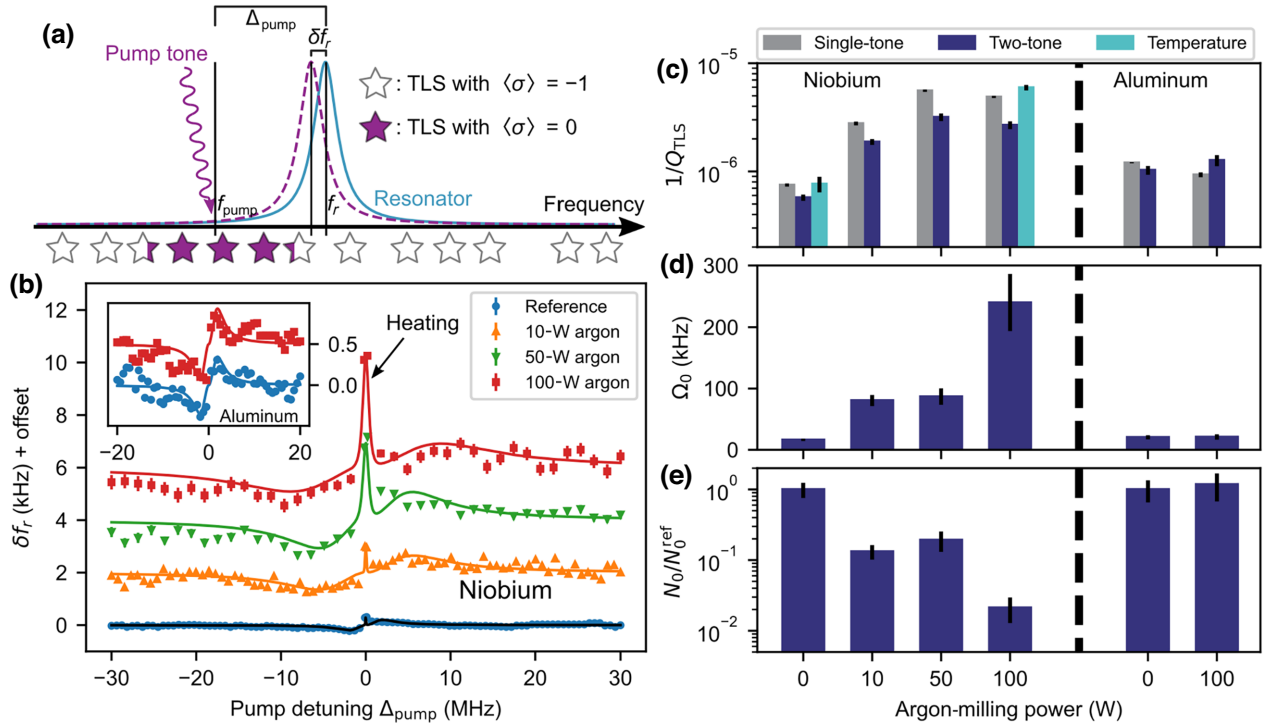
FIG. 3. Two-tone saturation measurement results. (a) Schematic of the experiment, a uniform energy distribution of TLS defects (stars) are partially saturated with a microwave-frequency pump tone detuned with frequency Δ from the resonator. (b) The pump detuning is swept around the resonator frequency and the resulting shift in resonator frequency δf_r is plotted. The results of Res 2 are shown for the different argon-milling conditions on niobium and aluminum (inset). The data is offset on the y axis for improved visibility. The solid lines are fits with Eq. (3) with the addition of a center peak coming from self-heating of the sample. (c) Comparison of the TLS loss of Res 2 on each sample extracted with the probe power sweep (Fig. 1), the pump sweep (b), and a temperature sweep (Appendix C). (d) The average TLS coupling to the resonator expressed as the single-photon Rabi frequency extracted from the pump sweep fits. (e) The relative change in TLS density as a function of argon-milling power. All error bars are one standard deviation uncertainty in the fitting parameters.

$Q_{\mathrm{TLS}}^{\mathrm{ref}}(\Omega_0^{\mathrm{ref}})^2/(Q_{\mathrm{TLS}}\Omega_0^2)$, illustrated by Fig. 3(e), that would compensate the larger than observed losses (assuming no changes in the distribution of dipole orientations due to the milling). Furthermore, like the loss, the TLS dipole moments on the aluminum surface do not change after argon milling.

IV. DISCUSSION

The observed resilience of the aluminum devices to the argon-milling recipe could be one of the reasons why overlap JJ qubits fabricated entirely with aluminum have recently been demonstrated with lifetimes exceeding 0.1 ms [17]. Our results show that attempting a similar fabrication process with niobium would require additional care. The surface losses of argon-milled niobium could be removed with an optimized over etch during JJ top-electrode patterning, except for the small contact region of this top electrode with the niobium circuitry. A similar study would have to be performed for other promising superconducting materials like tantalum or titanium nitride [23,26,55].

Surface analysis on niobium samples reveals no change in the niobium suboxide composition due to argon milling. However, the surface roughness is reduced by a factor of 0.63, and a layered density change is observed, with traces of Si throughout the entire oxide thickness. NbO is present at the niobium side of the metal-oxide interface in both reference and argon-milled samples. We hypothesize that the additional residual losses may come from excess quasiparticles due to magnetic impurities (interstitial oxygen and oxygen vacancies in $\mathrm{Nb_2O_5}$ are known to have net magnetization) in the structurally altered $\mathrm{Nb_2O_5}$ layer observed after argon milling [44,45]. Alternative hypotheses like proximity effects, or short-lived TLSs (with greatly enhanced n_c) coming from the metallic NbO seem less likely based on the lack of correlation between NbO concentration and argon-milling power in Fig. 2(f) and the absence of significant change in critical temperature measurements between reference and argon-milled niobium illustrated by Fig. 6(a) in Appendix C. To verify our hypothesis, magnetic impurities at the niobium surface could be further investigated in future work with on-chip electron spin resonance techniques [56], point contact

tunnelling spectroscopy [41], or flux temperature dependencies of superconducting quantum interference device (SQUID) loops [57].

After argon milling, TLS losses at the niobium surface increase considerably. Two-tone saturation experiments reveal a 15-fold increase in electrical dipole moment of the average TLS and a corresponding reduction in the density of defects with more than an order of magnitude. We speculate that, on a microscopic scale, the average tunnel defect changes from many single-charged atoms to fewer but larger clusters of collective atom motion [58] due to the additional argon-milling surface damage. The increased dipole moment is therefore likely a combination of larger defect size and effective charge. The AFM data corroborate this observation, where the surface peaks and valleys also increase in area and reduce in number. Alternatively, the presence of Si in the niobium oxide could potentially form new types of TLS with increased dipole moments. However, Si is also present after argon milling on aluminum devices, where no change in dipole moment is observed. Additionally, the amount of incorporated silicon should scale with the argon-milling power used, while the extracted defected density shown by Fig. 3(e) decreases with milling power.

V. CONCLUSION

We study the impact of argon milling on two different superconductors: niobium and aluminum. Niobium resonators show an order of magnitude increase in microwave loss; both the TLS and residual loss components increase as a function of argon-milling power. Aluminum is resilient against the same milling conditions. XPS analysis shows no change in the niobium suboxide concentrations, while STEM images reveal an altered niobium oxide with a layered structure of predominantly Nb_2O_5 after argon milling. Two-tone spectroscopy measurements show a 15-fold increase in average TLS dipole moment, while AFM shows reduced roughness and enlarged topographical peak and valley areas. We speculate that the residual losses come from paramagnetic interstitial oxygen and oxygen vacancies inside the Nb_2O_5, and the TLSs are formed by the combined motion of larger clusters of atoms. Removal of the amorphous niobium oxide layer with a short dry etch effectively removes all argon-milling-induced losses, showing a path towards foundry-compatible qubit fabrication with overlap JJs and niobium circuitry. Our results illustrate the importance of material and fabrication process co-optimization and the presented study method of combined loss characterization and surface analysis on superconducting resonators helps with the identification of the critical loss mechanisms in superconducting circuits.

APPENDIX A: EXPERIMENTAL SETUP

All microwave measurements reported in this work are performed inside a Bluefors LD dilution refrigerator, with the devices anchored to the 10-mK mixing chamber. Sample holders, cables, and connectors are all carefully tested for magnetic fields and extra cryoperm magnetic shielding around the samples is used. Figure 4 shows a schematic of the entire measurement setup where we can switch
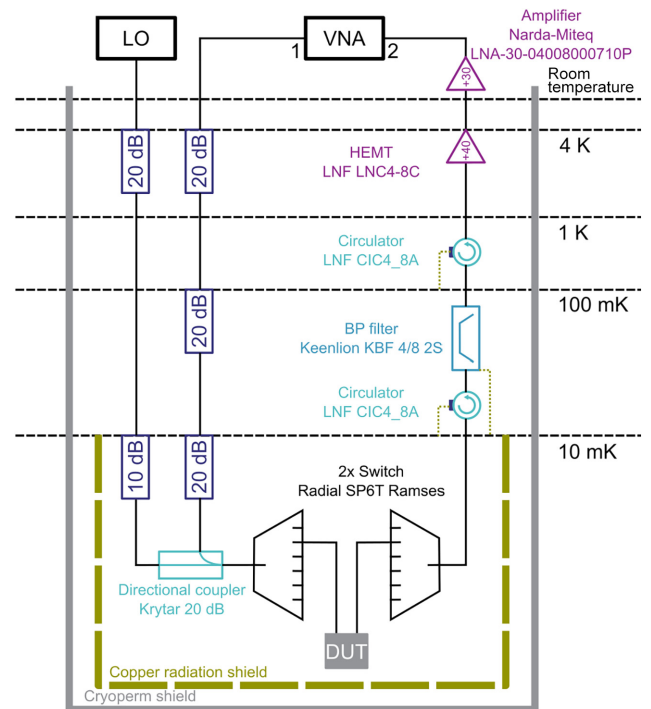

FIG. 4.   Schematic of the experimental setup used in this work.

between six different samples via mechanical switches connected to one input and one output line.

We use the Keysight P5004A streamline USB VNA to probe the resonators and the Keysight M9347A local oscillator (LO) to generate the pump tone signals.

APPENDIX B: CAVITY-COUPLED RESONATOR

The samples measured in this work are silicon chips of dimension 7×4.3 mm^2 with six different planar LER structures as shown by the microscope picture in Fig. 5(a). The chip is placed inside an aluminum cavity without adhesive or wire bonds, as illustrated by Fig. 5(b), including two I/O ports on the side. Nonmagnetic sub miniature version A (SMA) panel mount connectors can be screwed onto the cavity ports and copper spacers (not shown) can be used to tune the center pin insertion depth. The cavity's lowest frequency TE$_{101}$ mode is excited and read out via these I/O ports and is in turn coupled wirelessly to the resonator structures on the chip. Resonator designs are discussed in more detail by Ref. [15].
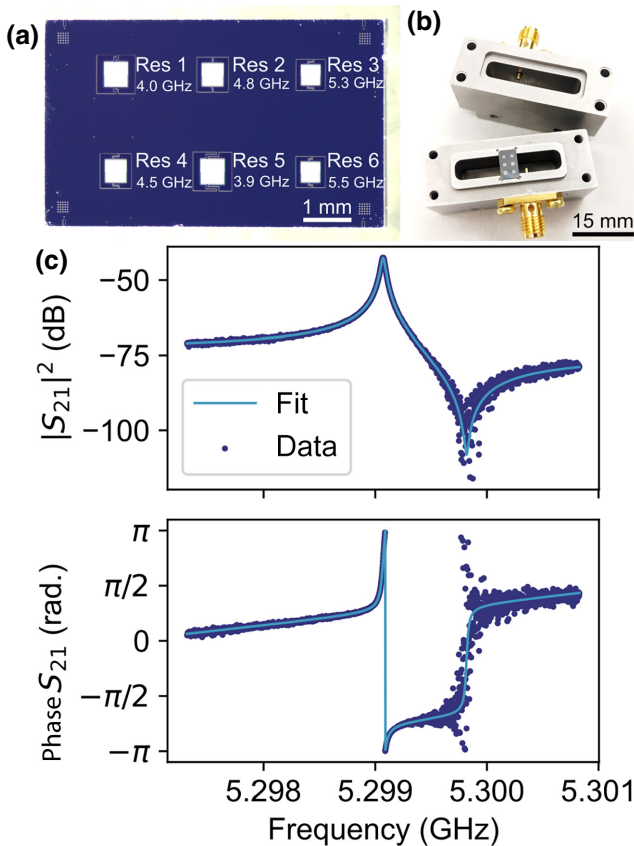

FIG. 5. Microscope picture of a silicon chip with six different superconducting lumped-element resonator designs (a). The chip is loaded inside an aluminum cavity (b) with adjustable input/output pins and a TE$_{101}$ mode at 8 GHz, facilitating under-coupled readout. (c) Example S_{21} trace measured (magnitude and phase) with the VNA and fitted with Eq. (B4).

Fitting model

The cavity-coupled resonator system is described by the Hamiltonian given by Eq. (B1) (including the rotating wave approximation), with $f_c = \omega_c/2\pi \approx 8$ GHz the cavity TE$_{101}$ resonance frequency, $f_r = \omega_r/2\pi \approx 5$ GHz the LER resonance frequency, and $g/2\pi \approx 50$ MHz the coupling rate between cavity and resonator. The creation and annihilation operator commutation relations are $[\hat{a}, \hat{a}^\dagger] = 1$ and $[\hat{b}, \hat{b}^\dagger] = 1$ for the cavity TE$_{101}$ mode and resonator mode, respectively.

$$\hat{H} = \hbar\omega_c \hat{a}^\dagger \hat{a} + \hbar\omega_r \hat{b}^\dagger \hat{b} + \hbar g(\hat{a}\hat{b}^\dagger + \hat{a}^\dagger \hat{b}) \quad (B1)$$

The coupling from the resonators on the chip to the I/O ports is assumed to be entirely mediated via the cavity mode, and any direct coupling between the small I/O port pins to the small resonator structures is neglected. The time-domain Langevin equations describing these input-output relations are given by Eq. (B2), where κ_A is the coupling rate to I/O port A, κ_B is the coupling rate to the I/O port B, γ_c is the internal loss rate of the cavity, and γ_r is the internal loss rate of the resonator [59],

$$\frac{d\hat{a}}{dt} = \frac{-i}{\hbar}[\hat{a}, \hat{H}] - \frac{\kappa_A + \kappa_B + \gamma_c}{2}\hat{a} + \sqrt{\kappa_A}\hat{A}_{\text{in}} + \sqrt{\kappa_B}\hat{B}_{\text{in}}$$

$$\frac{d\hat{b}}{dt} = \frac{-i}{\hbar}[\hat{b}, \hat{H}] - \frac{\gamma_r}{2}\hat{b}. \quad (B2)$$

At ports A and B, the boundary conditions $\left(\hat{A}_{\text{in}} + \hat{A}_{\text{out}} = \sqrt{\kappa_A}\hat{a}\right)$ and $\left(\hat{B}_{\text{in}} + \hat{B}_{\text{out}} = \sqrt{\kappa_B}\hat{b}\right)$ hold. This set of equations can be solved using Fourier transformation and results in the following Eq. (B3) for the transmission scattering parameter S_{21}, where we assume symmetrical I/O coupling $\kappa_A = \kappa_B = \kappa$ and negligible losses of the superconducting cavity walls (high purity aluminum) $\gamma_c \ll \kappa$. We define $\Delta_c = \omega - \omega_c$ and $\Delta_r = \omega - \omega_r$.

$$S_{21} = \left.\frac{B_{\text{out}}}{A_{\text{in}}}\right|_{B_{\text{in}}=0} = \frac{\kappa}{\kappa - i\Delta_c}$$
$$\times \left(1 + \frac{g^2}{(\kappa - i\Delta_c)(\gamma_r/2 - i\Delta_r) + g^2}\right) \quad (B3)$$

In the regime $\Delta_c \gg g, \kappa \gg \gamma_r, \Delta_r$ we can define the effective coupling rate from the perspective of the resonator as $\kappa_{\text{eff}} = (g^2/(\omega_r - \omega_c)^2)\kappa$ and approximate Eq. (B3) as

$$S_{21} \approx \frac{-i\kappa}{\Delta_c} + \frac{i\kappa_{\text{eff}}}{\omega - \tilde{\omega}_r + i(2\kappa_{\text{eff}} + \gamma_r/2)}$$
$$\text{with} \quad \tilde{\omega}_r = \omega_r + \frac{g^2}{\omega_r - \omega_c}. \quad (B4)$$

The experimental data are measured with the VNA through the cryostat input and output lines. We account for

TABLE II. Experimentally extracted coupling rates between the on-chip resonators and the cavity TE$_{101}$ mode as shown in Fig. 5.

Resonator name	Res 1	Res 2	Res 3	Res 4	Res 5	Res 6
$g/2\pi$ (MHz)	55	30	25	45	35	40

impedance mismatches, unknown attenuation and/or gain, and phase shifts in the fitting formula, from which we then extract the two parameters of interest ω_r and $\kappa_{\text{tot}} = 2\kappa_{\text{eff}} + \gamma_r$.

Additionally, we adjust the I/O pins for weak coupling $\kappa_{\text{eff}} \ll \gamma_r$ such that the loaded full-width-half-maximum linewidth is entirely determined by the internal losses ($\kappa_{\text{tot}} \approx \gamma_r$). Figure 5(c) illustrates the fitting model applied to experimental data, including the distinctive "peak and dip" in the magnitude plot, a consequence of the interference between the cavity component and the resonator component. The weak-coupling regime makes measurements at low powers slow and is currently a significant drawback of this type of cavity-coupled resonator system, compared to hanger-type CPW resonators coupled to a feedline [28].
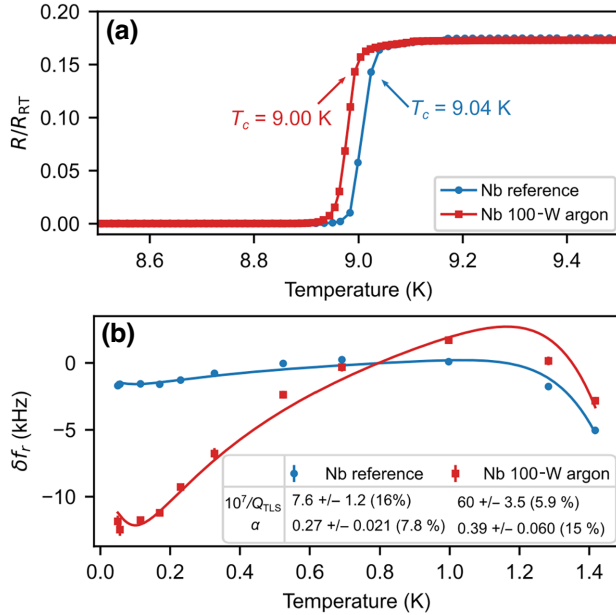

FIG. 6. Temperature dependences of reference niobium and argon-milled niobium. (a) Resistance, normalized to the room temperature resistance, measured with transport bridge structures processed identically to the measured resonator chips. The critical temperature T_c is extracted from the point in the superconductivity transition where the resistance is 90% of the resistance at 10 K. (b) Resonance frequency of Res 2 on each sample as function of temperature. Solid lines are fits with Eq. (C1) and corresponding fitting parameters for the TLS loss ($1/Q_{\text{TLS}}$) and kinetic inductance ratio (α) are added to the legend with their respective standard deviations.

Photon number extraction

The number of photons inside the resonator due to applied input microwaves is calculated from Eq. (B2) and is approximately given by Eq. (B5), with $P_{\text{in}} = \left\langle A_{\text{in}}^\dagger A_{\text{in}} \right\rangle \hbar\omega_r$ the microwave power arriving at port A of the cavity,

$$\bar{n} = \left\langle \hat{b}^\dagger \hat{b} \right\rangle \approx \frac{P_{\text{in}}}{\hbar\omega_r} \frac{4\kappa_{\text{eff}}}{(2\kappa_{\text{eff}} + \gamma_r)^2 + 4(\omega - \omega_r)^2}. \quad (B5)$$

The photon number estimation depends on the attenuation of the input line of the cryostat ($P_{\text{in}} = G_{\text{in}}P_{\text{VNA}}$) and the coupling rate of the resonator κ_{eff}. The input attenuation of the VNA input line is estimated as $G_{\text{in}} = -94$ dB and $G_{\text{in}} = -44$ dB for the LO pump line, based on the results of other experiments performed with superconducting qubits in the same cryostat where photon numbers could be resolved (data not included but available upon request). The effective coupling rate to the resonators is estimated experimentally by measuring the resonator linewidths in the overcoupled case $\kappa_{\text{eff}} = \kappa g^2/\Delta^2 \gg \gamma_r$ when the I/O pins are fully inserted into the cavity. From these measurements, the coupling g for each resonator design is extracted and summarized in Table II.

These reported values for g and G_{in} are used throughout this entire work and are assumed to be identical for different cooldowns and different samples (same designs and cavity dimensions). Potential errors on the photon number estimation due to incorrect input line attenuation or inaccurate coupling rate values would not change any conclusions drawn in this work.

APPENDIX C: TEMPERATURE DEPENDENCIES

Two transport bridge structures ($L \times W \times H = 20 \times 0.2 \times 0.1$ μm^3), from the same 300-mm wafer as the resonator chips measured in this work, are prepared with the reference and 100-W argon recipes. No significant impact of the milling on the superconducting properties of the niobium are found. Figure 6(a) illustrates the superconducting critical temperature at 9 K for both samples at zero applied field. These measurements are repeated at different applied magnetic fields from which the Ginzburg-Landau

TABLE III. Comparison of the superconducting parameters of thin-film niobium transport bridge structures treated with the reference or 100-W argon-milling post-processing recipes. We report the critical temperature (T_c), the GL coherence length ($\xi(T = 0)$), and the electron mean free path (l_{el}).

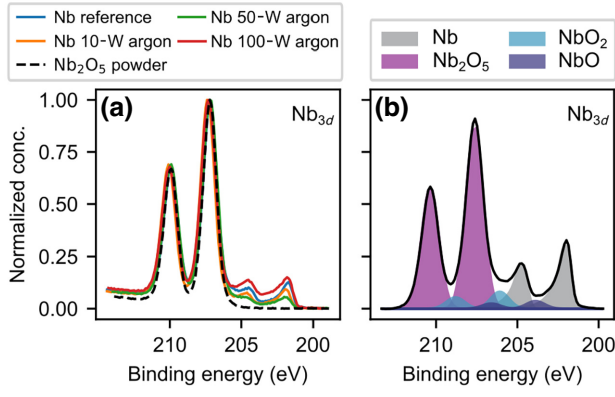|	Niobium reference	Niobium 100-W argon
T_c (K)	9.04	9.00
$\xi(T = 0)$ (nm)	11.6	12.3
l_{el} (nm)	4.84	5.44

FIG. 7.   XPS spectra at the Nb_{3d} binding energies. (a) The data presented correspond to blanket niobium samples (subjected to different argon-milling conditions) and a high purity ($>99.99\%$) Nb_2O_5 powder for tool calibration. (b) Example of peak fitting with mixed Gaussian-Lorentzian peaks (background subtracted), adjustable mixing percentage, width, and intensity is done on all experimental data to extract the relative suboxide concentrations reported in the main text Fig. 2(f).

(GL) coherence lengths $\xi(T = 0)$ are extracted. The electron mean free path l_{el} is calculated in the dirty limit using the BCS coherence length $\xi_0 = 38$ nm. These measurements are carried out at the Physics Department of KU Leuven and the extracted parameter values are presented in Table III.

Figure 6(b) compares the Res 2 resonance frequency shift as a function of temperature on the niobium reference sample and the 100-W argon-milled sample. The temperature is controlled and recorded via a mixing chamber heater and temperature sensor. The resonance frequency temperature dependence is governed by TLS and quasiparticle contributions according to Eq. (C1) [33],

$$\delta f_r(T) = \frac{f_r}{\pi Q_{TLS}} \text{Re} \left[\Psi \left(\frac{1}{2} - \frac{hf}{j\,2\pi k_B T} \right) - \ln \left(\frac{hf}{2\pi k_B T} \right) \right] - \frac{\alpha f_r}{2} \frac{X_S(T) - X_S(0)}{X_S}, \quad (C1)$$

with Ψ the digamma function, α the kinetic inductance fraction, and X_S the surface inductance. In the local or dirty limit, the surface impedance is given by [33]

$$Z_S = R_S + jX_S = \frac{j\,\mu_0\omega_r}{\sqrt{(\omega_r l_{el}/\sigma_n v_F \lambda_0^2)(\sigma_2(T) + j\,\sigma_1(T))}}, \quad (C2)$$

with v_F the Fermi velocity, λ_0 the London penetration depth, and $\sigma_1(T)/\sigma_n$ and $\sigma_2(T)/\sigma_n$ given by the Mattis-Bardeen integrals [60]. These can be evaluated in an analytical form in the regime of interest where the superconducting gap is large $\Delta_0 \gg \hbar\omega_r,\ k_B T$ [33],

$$\frac{\sigma_1(T)}{\sigma_n} = \frac{4\Delta_0}{\hbar\omega} e^{-(\Delta_0/k_B T)} \sinh\left(\frac{\hbar\omega}{2k_B T}\right) K_0\left(\frac{\hbar\omega}{2k_B T}\right) \quad (C3)$$

$$\frac{\sigma_2(T)}{\sigma_n} = \frac{\pi\Delta_0}{\hbar\omega}\left(1 - \sqrt{\frac{2\pi k_B T}{\Delta_0}} e^{-(\Delta_0/k_B T)} \right.$$
$$\left. - 2e^{-(\Delta_0/k_B T)}e^{-\hbar\omega/2k_B T}I_0\left(\frac{\hbar\omega}{2k_B T}\right)\right), \quad (C4)$$

with I_0 and K_0 the zeroth-order modified Bessel functions of the first and second kind, respectively.

The fits in Fig. 6(b) are made using Eqs. (C1)–(C4) with free fitting parameters $1/Q_{TLS}$ and α.
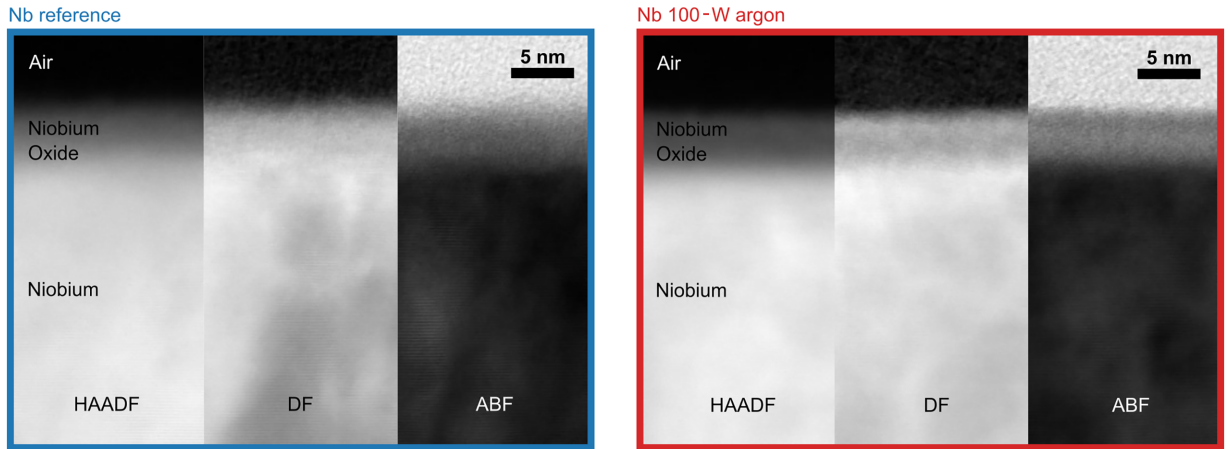

FIG. 8.   STEM images of a cross section at the niobium-air interface for a reference sample (a) and a sample subjected to the previously described 100-W argon-milling recipe (b). Scattered electrons are detected with three modes: high-angle annular dark field (HAADF), medium-angle dark field (DF), and low-angle annular bright field (ABF).
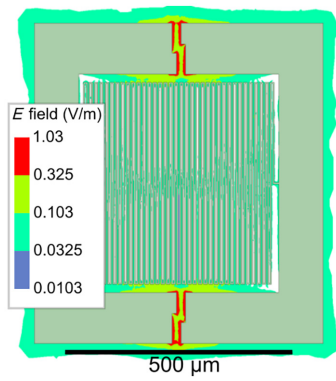
FIG. 9.　Simulated electric field distribution of Res 2 for a total energy of one resonant photon at 4.8 GHz.

APPENDIX D: SURFACE ANALYSIS

XPS

Multiple XPS measurements are carried out using an Ulvac-Phi VersaProbe III instrument and an Ulvac-Phi QUANTES instrument at Imec. On the QUANTES tool, the measurements are performed under an angle of 45° (more surface sensitive) and 90° (more bulk sensitive) using a monochromatized photon beam of 1486.6 eV and a spot size of 50 μm. With the VersaProbe III instrument the analysis is done with the same 1486.6 eV photon beam under a 45° angle, a spot size of 100 μm, and surface cleaning with a gas cluster ion beam (GCIB) sputter gun. We perform XPS on the niobium surface of the samples (resonator chips and blanket niobium chips) prepared with the previously described range of argon-milling powers (reference, 10, 50, and 100 W). From the Nb_{3d} spectra, the relative concentrations of Nb_2O_5, NbO_2, and NbO are extracted with a combined fit of mixed Gaussian-Lorentzian doublet peaks at about 5.7, 4.2, and 2.0 eV above the Nb metal binding energy, in agreement with the values given in Refs. [61,62]. The metallic Nb peak is fitted with an asymmetric Gaussian-Lorentzian doublet with an asymmetry parameter determined by a reference measurement of clean (sputtered) metallic Nb film (Fig. 7).

We attempt to find evidence for interstitial oxygen in the O_{1s} peak, where this could potentially show up as side peaks in the XPS spectrum. However, after careful surface cleaning with GCIB for the removal of any adsorbed carbon and hydrogen (whose oxides typically have different binding energies), no significant changes in the O_{1s} peak as function of argon-milling conditions is observed.

STEM

The specimens are capped with carbon at room temperature for FIB lift-out extraction in a Helios 450Hp. The images are taken with the Titan G2 60-300 operated at 200 kV (Fig. 8).

The brightness of the HAADF images is, to first order, proportional to $\langle Z \rangle^2$, with Z the atomic number, and is also linearly dependent on specimen thickness. The EDS curves Figs. 2(a) and 2(b) show traces of silicon inside the niobium oxide after the argon-milling treatment. The atomic number of Si ($Z = 14$) lies between those of Nb ($Z = 41$) and O ($Z = 8$), and the Si EDS content spans the entire oxide thickness, so we do not believe it contributes to the observed layers in the 100-W argon sample. The layers are also clearly visible in medium-angle and low-angle STEM images (contrast sensitive to changes in density and crystallinity), which indicates a structural difference rather than a compositional difference between the layers seen in the oxide. The surface roughness (along the thickness of the FIB sample) also plays a role in the visibility of such thin layers. Images taken on a rougher region of a 100-W argon-milled sample no longer show the presented layered oxide (data not included, but available upon request).

AFM

The AFM measurements shown in Figs. 2(e) and 2(g) are taken on the niobium surface of the resonator structures with the ICON PT tool using a OMCL-AC160TS-R3 probe.

APPENDIX E: TLS DIPOLE MOMENT ESTIMATION

We numerically simulate the electric field distribution of the Res 2 design using the eigenmode solver of ANSYS HFSS with a total field energy of one resonant photon $hf_r \approx 3.18 \times 10^{-24}$ J. The extracted field strength ranges across the device from 0.01 to 1 V/m (Fig. 9). We can estimate the average TLS dipole moment using these field values as $d = h\Omega_0/E_{(\bar{n}=1)}$ as tabulated in Table IV. Despite the uncertainties in the photon number estimation, and crude

TABLE IV.　Single-photon Rabi frequencies (Ω_0) of the average TLS defect for each sample measured with the two-tone spectroscopy technique described in the main text (Fig. 3). The error values correspond to one standard deviation uncertainty in the extracted fitting parameter Ω_0.

	Al reference	Al 100-W argon	Nb reference	Nb 10-W argon	Nb 50-W argon	Nb 100-W argon
Ω_0 (kHz)	20.4 ± 3.4	20.9 ± 4.3	16.2 ± 1.9	80.4 ± 9.0	86.8 ± 13	240 ± 46
[a]d/e (nm)	0.84	0.86	0.67	3.3	3.6	9.9

[a]For the electric field value $E = 0.1$ V/m (see Fig. 9).

approximations, we extract reasonable values for the TLS dipole moments [55,63,64].

[1] N. P. de Leon, K. M. Itoh, D. Kim, K. K. Mehta, T. E. Northup, H. Paik, B. S. Palmer, N. Samarth, S. Sangtawesin, and D. W. Steuerman, Materials challenges and opportunities for quantum computing hardware, Science **372,** eabb2823 (2021).

[2] S. E. de Graaf, S. Un, A. G. Shard, and T. Lindström, Chemical and structural identification of material defects in superconducting quantum circuits, Mater. Quantum Technol. **2,** 032001 (2022).

[3] C. Müller, J. H. Cole, and J. Lisenfeld, Towards understanding two-level-systems in amorphous solids: insights from quantum circuits, Rep. Prog. Phys. **82,** 124501 (2019).

[4] W. A. Phillips, Two-Level States in Glasses, (1987).

[5] P. V. Klimov, *et al.*, Fluctuations of Energy-Relaxation Times in Superconducting Qubits, Phys. Rev. Lett. **121,** 090502 (2018).

[6] C. Müller, J. Lisenfeld, A. Shnirman, and S. Poletto, Interacting two-level defects as sources of fluctuating high-frequency noise in superconducting circuits, Phys. Rev. B **92,** 035442 (2015).

[7] T. Thorbeck, A. Eddins, I. Lauer, D. T. McClure, and M. Carroll, Two-Level-System Dynamics in a Superconducting Qubit Due to Background Ionizing Radiation, PRX Quantum **4,** 020356 (2023).

[8] J. Gao, M. Daal, J. M. Martinis, A. Vayonakis, J. Zmuidzinas, B. Sadoulet, B. A. Mazin, P. K. Day, and H. G. Leduc, A semiempirical model for two-level system noise in superconducting microresonators, Appl. Phys. Lett. **92,** 212504 (2008).

[9] G. Calusine, A. Melville, W. Woods, R. Das, C. Stull, V. Bolkhovsky, D. Braje, D. Hover, D. K. Kim, X. Miloshi, D. Rosenberg, A. Sevi, J. L. Yoder, E. Dauler, and W. D. Oliver, Analysis and mitigation of interface losses in trenched superconducting coplanar waveguide resonators, Appl. Phys. Lett. **112,** 062601 (2018).

[10] W. Woods, G. Calusine, A. Melville, A. Sevi, E. Golden, D. K. Kim, D. Rosenberg, J. L. Yoder, and W. D. Oliver, Determining Interface Dielectric Losses in Superconducting Coplanar-Waveguide Resonators, Phys. Rev. Appl. **12,** 014012 (2019).

[11] A. Melville, G. Calusine, W. Woods, K. Serniak, E. Golden, B. M. Niedzielski, David Kiewook Kim, A. Sevi, J. L. Yoder, E. A. Dauler, and W. D. Oliver, Comparison of dielectric loss in titanium nitride and aluminum superconducting resonators, Appl. Phys. Lett. **117,** 124004 (2020).

[12] D. S. Wisbey, J. Gao, M. R. Vissers, F. C. S. da Silva, J. S. Kline, L. Vale, and D. P. Pappas, Effect of metal/substrate interfaces on radio-frequency loss in superconducting coplanar waveguides, J. Appl. Phys. **108,** 093918 (2010).

[13] J. Goetz, F. Deppe, M. Haeberlein, F. Wulschner, C. W. Zollitsch, S. Meier, M. Fischer, P. Eder, E. Xie, K. G. Fedorov, E. P. Menzel, A. Marx, and R. Gross, Loss mechanisms in superconducting thin film microwave resonators, J. Appl. Phys. **119,** 015304 (2016).

[14] A. Nersisyan, *et al.*, in *2019 IEEE International Electron Devices Meeting (IEDM)* (2019), pp. 31.1.1–31.1.4.

[15] J. Verjauw, *et al.*, Investigation of Microwave Loss Induced by Oxide Regrowth in High-Q Niobium Resonators, Phys. Rev. Appl. **16,** 014018 (2021).

[16] M. V. P. Altoé, *et al.*, Localization and mitigation of loss in niobium superconducting circuits, PRX Quantum **3,** 020312 (2022).

[17] J. Verjauw, R. Acharya, J. Van Damme, Ts. Ivanov, D. Perez Lozano, F. A. Mohiyaddin, D. Wan, J. Jussot, A. M. Vadiraj, M. Mongillo, M. Heyns, I. Radu, B. Govoreanu and A. Potočnik, Path toward manufacturable superconducting qubits with relaxation times exceeding 0.1 ms, Npj Quantum Inf. **8,** 1 (2022).

[18] X. Wu, J. L. Long, H. S. Ku, R. E. Lake, M. Bal, and D. P. Pappas, Overlap junctions for high coherence superconducting qubits, Appl. Phys. Lett. **111,** 032602 (2017).

[19] A. Stehli, J. D. Brehm, T. Wolz, P. Baity, S. Danilin, V. Seferai, H. Rotzinger, A. V. Ustinov, and M. Weides, Coherent superconducting qubits from a subtractive junction fabrication process, Appl. Phys. Lett. **117,** 124005 (2020).

[20] A. Dunsworth, *et al.*, Characterization and reduction of capacitive loss induced by sub-micron Josephson junction fabrication in superconducting qubits, Appl. Phys. Lett. **111,** 022601 (2017).

[21] C. M. Quintana, *et al.*, Characterization and reduction of microfabrication-induced decoherence in superconducting quantum circuits, Appl. Phys. Lett. **105,** 062601 (2014).

[22] M. Mergenthaler, C. Müller, M. Ganzhorn, S. Paredes, P. Müller, G. Salis, V. P. Adiga, M. Brink, M. Sandberg, J. B. Hertzberg, S. Filipp, and A. Fuhrer, Effects of surface treatments on flux tunable transmon qubits, Npj Quantum Inf. **7,** 1 (2021).

[23] A. P. M. Place, *et al.*, New material platform for superconducting transmon qubits with coherence times exceeding 0.3 milliseconds, Nat. Commun. **12,** 1779 (2021).

[24] C. Wang, *et al.*, Towards practical quantum computers: Transmon qubit with a lifetime approaching 0.5 milliseconds, Npj Quantum Inf. **8,** 3 (2022).

[25] J. B. Chang, M. R. Vissers, A. D. Corcoles, M. Sandberg, J. Gao, D. W. Abraham, J. M. Chow, J. M. Gambetta, M. B. Rothwell, G. A. Keefe, M. Steffen, and D. P. Pappas, Improved superconducting qubit coherence using titanium nitride, Appl. Phys. Lett. **103,** 012602 (2013).

[26] C. R. H. McRae, H. Wang, J. Gao, M. R. Vissers, T. Brecht, A. Dunsworth, D. P. Pappas, and J. Mutus, Materials loss measurements using superconducting microwave resonators, Rev. Sci. Instrum. **91,** 091101 (2020).

[27] M. S. Khalil, M. J. A. Stoutimore, F. C. Wellstood, and K. D. Osborn, An analysis method for asymmetric resonator transmission applied to superconducting devices, J. Appl. Phys. **111,** 054510 (2012).

[28] S. Probst, F. Song, P. Bushev, A. Ustinov, and M. Weides, Efficient and robust analysis of complex scattering data under noise in microwave resonators, Rev. Sci. Instrum. **86,** 024706 (2014).

[29] M. Newville, T. Stensitzki, D. B. Allen, and A. Ingargiola, LMFIT: Non-Linear Least-Square Minimization and Curve-Fitting for Python, (2014).

[30] N. Kirsh, E. Svetitsky, A. L. Burin, M. Schechter, and N. Katz, Revealing the nonlinear response of a tunneling two-level system ensemble using coupled modes, Phys. Rev. Mater. **1**, 012601 (2017).

[31] T. Capelle, E. Flurin, E. Ivanov, J. Palomo, M. Rosticher, S. Chua, T. Briant, P.-F. Cohadon, A. Heidmann, T. Jacqmin, and S. Deléglise, Probing a Two-Level System Bath via the Frequency Shift of an Off-Resonantly Driven Cavity, Phys. Rev. Appl. **13**, 034022 (2020).

[32] G. Andersson, A. L. O. Bilobran, M. Scigliuzzo, M. M. de Lima, J. H. Cole, and P. Delsing, Acoustic spectral hole-burning in a two-level system ensemble, Npj Quantum Inf. **7**, 15 (2021).

[33] J. Gao, phd, California Institute of Technology, 2008.

[34] A. Bilmes, A. Megrant, P. Klimov, G. Weiss, J. M. Martinis, A. V. Ustinov, and J. Lisenfeld, Resolving the positions of defects in superconducting quantum bits, Sci. Rep. **10**, 3090 (2020).

[35] J. Lisenfeld, G. J. Grabovskij, C. Müller, J. H. Cole, G. Weiss, and A. V. Ustinov, Observation of directly interacting coherent two-level systems in an amorphous material, Nat. Commun. **6**, 6182 (2015).

[36] L. Faoro and L. B. Ioffe, Internal Loss of Superconducting Resonators Induced by Interacting Two-Level Systems, Phys. Rev. Lett. **109**, 157005 (2012).

[37] H. Wang, M. Hofheinz, J. Wenner, M. Ansmann, R. C. Bialczak, M. Lenander, E. Lucero, M. Neeley, A. D. O'Connell, D. Sank, M. Weides, A. N. Cleland, and J. M. Martinis, Improving the coherence time of superconducting coplanar resonators, Appl. Phys. Lett. **95**, 233508 (2009).

[38] J. M. Sage, V. Bolkhovsky, W. D. Oliver, B. Turek, and P. B. Welander, Study of loss in superconducting coplanar waveguide resonators, J. Appl. Phys. **109**, 063915 (2011).

[39] J. Halbritter, On the oxidation and on the superconductivity of niobium, Appl. Phys. Solids Surf. **43**, 1 (1987).

[40] C. Nico, T. Monteiro, and M. P. F. Graça, Niobium oxides and niobates physical properties: Review and prospects, Prog. Mater. Sci. **80**, 1 (2016).

[41] T. Proslier, J. F. Zasadzinski, L. Cooley, C. Antoine, J. Moore, J. Norem, M. Pellin, and K. E. Gray, Tunneling study of cavity grade Nb: Possible magnetic scattering at the surface, Appl. Phys. Lett. **92**, 212505 (2008).

[42] R. Barends, W. K.-G. Daalman, A. Endo, S. Zhu, T. Zijlstra, and T. M. Klapwijk, Frequency and quality factor of NbTiN/Au bilayer superconducting resonators, AIP Conf. Proc. **1185**, 152 (2009).

[43] M. Kharitonov, T. Proslier, A. Glatz, and M. J. Pellin, Surface impedance of superconductors with magnetic impurities, Phys. Rev. B **86**, 024514 (2012).

[44] T. Proslier, M. Kharitonov, M. Pellin, J. Zasadzinski, and A. Ciovati, Evidence of surface paramagnetism in niobium and consequences for the superconducting cavity surface impedance, IEEE Trans. Appl. Supercond. **21**, 2619 (2011).

[45] T. F. Harrelson, E. Sheridan, E. Kennedy, J. Vinson, A. T. N'Diaye, M. V. P. Altoé, A. Schwartzberg, I. Siddiqi, D. F. Ogletree, M. C. Scott, and S. M. Griffin, Elucidating the local atomic and electronic structure of amorphous oxidized superconducting niobium films, Appl. Phys. Lett. **119**, 244004 (2021).

[46] E. Sheridan, T. F. Harrelson, E. Sivonxay, K. A. Persson, M. V. P. Altoé, I. Siddiqi, D. F. Ogletree, D. I. Santiago, and S. M. Griffin, Microscopic Theory of Magnetic Disorder-Induced Decoherence in Superconducting Nb Films, arXiv:2111.11684.

[47] D. Bach, R. Schneider, D. Gerthsen, J. Verbeeck, and W. Sigle, EELS of niobium and stoichiometric niobium-oxide phases—Part I: Plasmon and near-edges fine structure, Microsc. Microanal. **15**, 505 (2009).

[48] X. Q. Jia, L. Kang, X. Y. Liu, Z. H. Wang, B. B. Jin, S. B. Mi, J. Chen, W. W. Xu, and P. H. Wu, High performance ultra-thin niobium films for superconducting hot-electron devices, IEEE Trans. Appl. Supercond. **23**, 4 (2013).

[49] C. T. Earnest, J. H. Béjanin, T. G. McConkey, E. A. Peters, A. Korinek, H. Yuan, and M. Mariantoni, Substrate surface engineering for high-quality silicon/aluminum superconducting resonators, Supercond. Sci. Technol. **31**, 125013 (2018).

[50] A. Corney, Optical resonance and two-level atoms: L. Allen, J.H. Eberly John Wiley, 1975, £10.80, Opt. Laser Technol. **8**, 281 (1976).

[51] L. Faoro and L. B. Ioffe, Interacting tunneling model for two-level systems in amorphous materials and its predictions for their dephasing and noise in superconducting microresonators, Phys. Rev. B **91**, 014201 (2015).

[52] S. E. de Graaf, L. Faoro, L. B. Ioffe, S. Mahashabde, J. J. Burnett, T. Lindström, S. E. Kubatkin, A. V. Danilov, and A. Ya. Tzalenchuk, Two-level systems in superconducting quantum devices due to trapped quasiparticles, Sci. Adv. **6**, eabc5055 (2020).

[53] R. Barends, J. Kelly, A. Megrant, D. Sank, E. Jeffrey, Y. Chen, Y. Yin, B. Chiaro, J. Mutus, C. Neill, P. O'Malley, P. Roushan, J. Wenner, T. C. White, A. N. Cleland, and J. M. Martinis, Coherent Josephson Qubit Suitable for Scalable Quantum Integrated Circuits, Phys. Rev. Lett. **111**, 080502 (2013).

[54] J. Lisenfeld, A. Bilmes, A. Megrant, R. Barends, J. Kelly, P. Klimov, G. Weiss, J. M. Martinis, and A. V. Ustinov, Electric field spectroscopy of material defects in transmon qubits, Npj Quantum Inf. **5**, 1 (2019).

[55] S. Kim, H. Terai, T. Yamashita, W. Qiu, T. Fuse, F. Yoshihara, S. Ashhab, K. Inomata, and K. Semba, Enhanced coherence of all-nitride superconducting qubits epitaxially grown on silicon substrate, Commun. Mater. **2**, 98 (2021).

[56] S. E. de Graaf, A. A. Adamyan, T. Lindström, D. Erts, S. E. Kubatkin, A. Ya. Tzalenchuk, and A. V. Danilov, Direct Identification of Dilute Surface Spins on Al_2O_3: Origin of Flux Noise in Quantum Circuits, Phys. Rev. Lett. **118**, 057703 (2017).

[57] S. Sendelbach, D. Hover, A. Kittel, M. Mück, J. M. Martinis, and R. McDermott, Magnetism in SQUIDs at Millikelvin Temperatures, Phys. Rev. Lett. **100**, 227006 (2008).

[58] V. Lubchenko and P. G. Wolynes, Intrinsic Quantum Excitations of Low Temperature Glasses, Phys. Rev. Lett. **87**, 4 (2001).

[59] D. F. Walls and G. J. Milburn, in *Quantum Optics*, edited by D. F. Walls, G. J. Milburn (Springer, Berlin, Heidelberg, 2008), pp. 127–141.

[60] D. C. Mattis and J. Bardeen, Theory of the Anomalous Skin Effect in Normal and Superconducting Metals, Phys. Rev. **111**, 412 (1958).

[61] M. Delheusy, A. Stierle, N. Kasper, R. P. Kurta, A. Vlad, H. Dosch, C. Antoine, A. Resta, E. Lundgren, and J. Andersen, X-ray investigation of subsurface interstitial oxygen at Nb/oxide interfaces, Appl. Phys. Lett. **92**, 101911 (2008).

[62] NIST XPS Database, Selected Element Search Result, https://srdata.nist.gov/xps/EngElmSrchQuery.aspx?EType =PE&CSOpt=Retri_ex_dat&Elm=Nb.

[63] J. M. Martinis, K. B. Cooper, R. McDermott, M. Steffen, M. Ansmann, K. D. Osborn, K. Cicak, S. Oh, D. P. Pappas, R. W. Simmonds, and C. C. Yu, Decoherence in Josephson Qubits from Dielectric Loss, Phys. Rev. Lett. **95**, 210503 (2005).

[64] B. Sarabi, A. N. Ramanayaka, A. L. Burin, F. C. Wellstood, and K. D. Osborn, Projected Dipole Moments of Individual Two-Level Defects Extracted Using Circuit Quantum Electrodynamics, Phys. Rev. Lett. **116**, 167002 (2016).